Taylor & Francis
Taylor & Francis Group

RESEARCH PAPER

Check for updates

PA2G4/EBP1 ubiquitination by PRKN/PARKIN promotes mitophagy protecting neuron death in cerebral ischemia

Inwoo Hwang[a,b], Byeong-Seong Kim[a,b], Ho Yun Lee[c], Sung-Woo Cho[d], Seung Eun Lee[e], and Jee-Yin Ahn[a,b,f]

aDepartment of Molecular Cell Biology, Single Cell Network Research Center, Sungkyunkwan University School of Medicine, Suwon, Korea; bSingle Cell Network Research Center, Sungkyunkwan University School of Medicine, Suwon, Korea; cDepartment of Radiology and Center for Imaging Science, Samsung Medical Center, Sungkyunkwan University School of Medicine, Seoul, South Korea; dDepartment of Biochemistry and Molecular Biology, University of Ulsan, College of Medicine, Seoul, Korea; eResearch Animal Resources Center, Korea Institute of Science and Technology, Seongbuk-gu, Republic of Korea; fSamsung Biomedical Research Institute, Samsung Medical Center, Seoul, Korea

ABSTRACT

Cerebral ischemia induces massive mitochondrial damage, leading to neuronal death. The elimination of damaged mitochondria via mitophagy is critical for neuroprotection. Here we show that the level of PA2G4/EBP1 (proliferation-associated 2G4) was notably increased early during transient middle cerebral artery occlusion and prevented neuronal death by eliciting cerebral ischemia-reperfusion (IR)-induced mitophagy. Neuron-specific knockout of Pa2g4 increased infarct volume and aggravated neuron loss with impaired mitophagy and was rescued by introduction of adeno-associated virus serotype 2 expressing PA2G4/EBP1. We determined that PA2G4/EBP1 is ubiquitinated on lysine 376 by PRKN/PARKIN on the damaged mitochondria and interacts with receptor protein SQSTM1/p62 for mitophagy induction. Thus, our study suggests that PA2G4/EBP1 ubiquitination following cerebral IR-injury promotes mitophagy induction, which may be implicated in neuroprotection.

Abbreviations: AAV: adeno-associated virus; ACTB: actin beta; BNIP3L/NIX: BCL2 interacting protein 3 like; CA1: Cornu Ammonis 1; CASP3: caspase 3; CCCP: carbonyl cyanide m-chlorophenyl hydrazone; DMSO: dimethyl sulfoxide; PA2G4/EBP1: proliferation-associated 2G4; FUNDC1: FUN14 domain containing 1; IB: immunoblotting; ICC: immunocytochemistry; IHC: immunohistochemistry; IP: immunoprecipitation; MCAO: middle cerebral artery occlusion; MEF: mouse embryonic fibroblast; OGD: oxygen-glucose deprivation; PRKN/PARKIN: parkin RBR E3 ubiquitin protein ligase; PINK1: PTEN induced kinase 1; RBFOX3/NeuN: RNA binding fox-1 homolog 3; SQSTM1/p62: sequestosome 1; TIMM23: translocase of inner mitochondrial membrane 23; TOMM20: translocase of outer mitochondrial membrane 20; TUBB: tubulin beta class I; WT: wild-type

Introduction

Cerebral ischemia is a leading cause of mortality and disability that produces selective neuronal death in the hippocampal CA1 layer [1], although only limited therapies are currently available. Ischemia promotes translational arrest and accumulation of polyubiquitinated proteins, indicating a metabolic shift from protein synthesis to protein degradation [2]. In the first 1–3 h following induction of ischemia, the functional integrity of the mitochondrial membrane is compromised, causing apoptosis and the release of CYCS (cytochrome c, somatic) and activation of caspases [3]. Continual mitochondrial impairment is a common consequence of cerebral ischemic insult progression. Mitophagy, also known as selective autophagy of mitochondria, is an important mechanism that eliminates damaged mitochondria, and thereby protects neurons against ischemic injury [4-7]. For instance, mdivi-1, a mitophagy inhibitor, abolished the reduction of mitochondrial markers, including TOMM20 (translocase of outer mitochondria membrane 20), but increased infarct volumes and neurologic deficit

after transient middle cerebral artery occlusion (MCAO) in mice [8]. Reinforced mitophagy is known to confer benefits for neuronal survival [9, 10]. These findings indicate that mitophagy activation may hold promise as a potential therapeutic strategy against brain ischemic injury [11]. However, the mechanisms underlying mitophagy in ischemic neurons are not fully uncovered.

There are three main mitophagy pathways in mammalian cells. These include PINK1 (PTEN induced putative kinase 1)-PRKN/PARKIN (a RING/HEC1 type E3 ligase)-mediated pathway and two PRKN-independent pathways, including BNIP3L/NIX (BCL2 interacting protein 3 like)-BCL2 (BCL2 apoptosis regulator)-BNIP3 (BCL2 interacting protein 3) and FUNDC1 (FUN14 domain containing 1) pathway. The PINK1-PRKN-dependent mitophagy is of particular concern as dysfunction of this pathway is associated with cerebral ischemic injury [12]. The activation of PINK1-PRKN-dependent mitophagy can ameliorate neuronal damage in the cortex and hippocampal CA1 region following cerebral ischemia and the clearing of damaged mitochondria [13,14].

In response to mitochondrial damage, PINK accumulates on the outer mitochondrial membrane (OMM), and recruits and activates PRKN to the damaged OMM regions. Activated PRKN ubiquitinates substrates in the OMM to subsequently recruit ubiquitin adaptor proteins and induce mitochondrial ubiquitination, thereby causing selective elimination of damaged mitochondria via autophagosome activity. [15]. Although selective autophagy machinery, including mitophagy, utilize ubiquitin chains as a molecular signal to recruit autophagy machinery and promote engulfment of damaged mitochondria into the autophagosome, little is understood concerning the downstream events of PINK-PRKN pathway in cerebral ischemia.

PA2G4/EBP1 is a critical controller for neuronal survival, differentiation, and axon regeneration after injury, contributing to multiple cellular signaling [16-18]. Two alternatively spliced PA2G4/EBP1 isoforms, p48 and p42, the latter of which lacks 54 amino acids at the N terminus, have been described, and their functions are distinctive in certain types of cancers. PA2G4/p48 is the predominant isoform and prevents neuronal apoptosis [19]. Silencing of PA2G4/EBP1 results in massive neuron loss, causing deregulation of epigenetic controllers, such as SUV39H1-DNMT1, and/or causing transcriptional deregulation during development and disease [18,20-22]. However, the role of PA2G4/EBP1 in IR-induced neuronal death is currently unknown. In this study, we found that PA2G4/EBP1 expression was transiently increased upon ischemic damage within 24 h in the hippocampus and prevented neuronal death, contributing to mitophagy induction. Moreover, we identified PA2G4/EBP1 as a neuronal substrate of PRKN E3 ligase while PA2G4/EBP1-K63 ubiquitination helped recruit SQSTM1, a protein involved in linking polyubiquitinated protein to the autophagic machinery, in the process of mitophagy. Thus, our study identified a neuroprotective effect of PA2G4/EBP1 as an important mediator of mitophagy to provide a biological rationale for the development of cerebral ischemia therapies to modulate the mitophagy process.

Results

PA2G4/EBP1 is upregulated and alleviates neuron loss after cerebral ischemic injury.

Because the loss of Pa2g4 elicits massive neuron loss in the brain and PA2G4/EBP1 plays a role in neuronal survival, we hypothesized that PA2G4/EBP1 may contribute to neuroprotection after brain cerebral ischemia–reperfusion (IR) injury. Upregulated expression of Pa2g4 was recorded in the publicly accessible database of stroke patients (GSE58294) [23] and under oxygen glutamate deprivation (GSE109233) [24], as well as in an in vitro model of cerebral ischemia (Figure 1A). To investigate the potent role of PA2G4/EBP1 in ischemic damage, we performed transient middle cerebral artery occlusion (MCAO) in mice. Interestingly, we found that mRNA and protein levels of Pa2g4 were highly upregulated within 24 h and then gradually diminished for 72 h. PA2G4/EBP1 levels were inversely correlated with those

of active CASP3 (caspase 3) or BAX, which are hallmarks of cell death [25] (Figure 1B). Immunohistochemistry (IHC) confirmed that, after MCAO, the most prominent change in PA2G4/EBP1 expression occurred in the Cornu Ammonis 1 (CA1) region of the mouse hippocampus rather than in the dentate gyrus or CA3 region. PA2G4/EBP1 immunostaining transiently increased after 24 h and diminished with time while notable neuron loss became apparent (Figures 1C and D). Thus, our data suggest that the transient upregulation of PA2G4/EBP1 expression prevents neural death, but with prolonged MCAO, PA2G4/EBP1 expression decreases and PA2G4/EBP1 no longer protects neurons.

PA2G4/EBP1 deficiency exacerbates IR brain injury.

To determine the physiological roles of PA2G4/EBP1 under ischemic damage, we generated forebrain-specific pa2g4-conditional knockout mice (CamKII-Cre; pa2g4$^{flox/flox}$; hereafter referred to as pa2g4-CKO) by crossing pa2g4$^{flox/flox}$ (hereafter referred to as control) with CANK2A/CaMKIIa-Cre driver [26,27]. Using mRNA expression and IHC analyses, we confirmed that Pa2g4 expression was successfully abolished in the hippocampus and cortex but not in the cerebellum (Figures S1A–C). We conducted cerebral IR injury in pa2g4-CKO and control mice (Figure 2A). PA2G4/EBP1 deficiency significantly exacerbated ischemic brain injury as revealed by a severe neuron loss in the CA1 region compared with that in MCAO-operated control mice (Figures 2B, C and Figure S1D). Moreover, the rate of neural death, quantified using active-CASP3 and transferase dUTP nick end labeling (TUNEL) staining, was notably increased in CA1 of pa2g4-CKO mice (Figure 2D). T2-weighted magnetic resonance imaging (MRI) allowed to visualize the damaged brain structure and quantify the brain infarct volume after IR, revealing that pa2g4-CKO mouse brains were more vulnerable to ischemic injury than control brains (Figure 2E). Accordingly, deficiency reduced the survival rate of mice compared with that of control mice after MCAO (p < 0.0001) (Figure 2F).

To demonstrate that the increased ischemic brain damage found in pa2g4-CKO mice was indeed due to a lack of PA2G4/EBP1 and that PA2G4/EBP1 is involved in neuroprotection, we generated adeno-associated virus serotype 2 (AAV2) that expressed GFP-PA2G4/EBP1 or GFP-MOCK and performed in vivo injections in the prospective IR injury site of pa2g4-CKO and control mice 5 days before MCAO (Figure 2G). This timing of viral injection enables AAV2 expression from day 1 after IR injury [28,29]. The success of the adenoviral delivery was verified using time series IHC and western blotting analyses of brain sections (Figures S1E–G). Expression of GFP-PA2G4/EBP1 significantly decreased the brain infarct volume after IR. Furthermore, the number of microtubule-associated protein 2 (MAP2)-positive neurons prominently increased in the brain of pa2g4-CKO mice expressing AAV2-GFP-PA2G4/EBP1, whereas neurons in the brain of pa2g4-CKO mice expressing AAV2-GFP-MOCK exhibited a largely reduced intensity of MAP2 staining after MCAO (Figures 2H and 2I). Accordingly, the reintroduction of PA2G4/EBP1 into pa2g4-CKO mice restored their movement following MCAO, whereas pa2g4-CKO mice
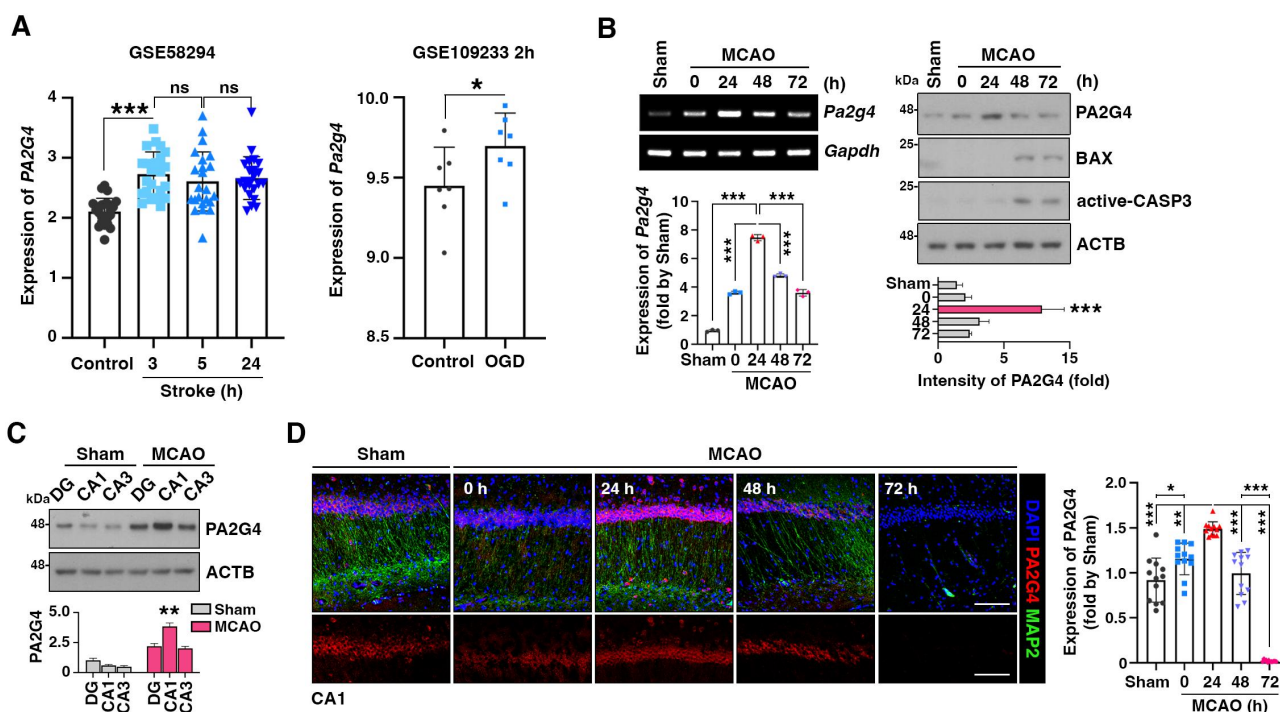
Figure 1. PA2G4 is upregulated and alleviates neuron loss after cerebral ischemic injury. (A) Expression of *PA2G4* in the human brain (left) or pericyte cells (right). Gene expression profiles were obtained from human brains 3, 5, and 24 h after stroke (NCBI GEO NO. GSE58294) and human pericyte cells after oxygen–glucose deprivation (OGD) for 2 h (NCBI GEO NO. GSE109233). (B) RNA (left) and protein (right) expression levels of PA2G4 were analyzed by qRT-PCR and immunoblotting, respectively, from wild-type mouse hippocampi 0, 24, 48, and 72 h after a 45-min MCAO. The relative fold changes of RNA expression were quantified and are shown in bar graphs (bottom). (C) Protein expression of PA2G4 was measured from the DG, CA1, and CA3 of the hippocampus by immunoblotting (top). The intensity of PA2G4 expression was quantified (bottom). (D) Mouse brains were isolated at the indicated time after MCAO, and immunohistochemistry was performed using anti-PA2G4 (red) and MAP2 (green) antibodies. Images showing the CA1 region were used to quantify the intensity of PA2G4 staining. The corresponding data are displayed as a bar graph (right panel). Scale bar: 50 μm. All data are presented as means ± standard errors of the mean (SEMs); *p < 0.05, **p < 0.005, ***p < 0.001. Student's two-tailed unpaired t-test (A, C) and one-way analysis of variance (ANOVA) followed by Bonferroni's post hoc test (A, B, D) were performed.

expressing GFP-control rarely showed motion (videos S1 and S2). Moreover, the number of terminal deoxynucleotidyl TUNEL-positive cells were markedly reduced in MCAO-operated *pa2g4*-CKO brains expressing AAV2-GFP-PA2G4/EBP1. In contrast, AAV2-GFP-MOCK expression could not prevent neuronal death in IR-injured *pa2g4*-CKO mouse brains (Figure 2J). The phenotypic rescue and neural protection observed after the reinstatement of PA2G4/EBP1 implies that depletion of PA2G4/EBP1 is the major cause of *pa2g4*-CKO mice vulnerability toward cerebral IR injury, suggesting a therapeutic role of PA2G4/EBP1 function in the ischemic brain.

PA2G4/EBP1 is required in IR-induced mitophagy.

During IR, mitophagy inhibition exacerbates brain injury, whereas stimulation of mitophagy is beneficial to neuronal survival in the rapid period of reperfusion [5,6,9,30]. Expression of PA2G4/EBP1 was upregulated at early time points after MCAO to alleviate neuron loss (Figures 1 and 2). Additionally, PA2G4/EBP1 was notably translocated from the cytoplasm to the mitochondria in the mouse brain after MCAO, whereas its nuclear localization was reduced (Figure 3A and Figure S2A). Therefore, we hypothesized that PA2G4/EBP1 contributed to the IR-induced mitophagy process. To test this hypothesis, we first elicited mitophagy by

treating primary cultured hippocampal neurons or SH-SY5Y neuronal cells with CCCP hydrazine, a mitochondria uncoupler. PA2G4/EBP1 was translocated to depolarized mitochondria as shown by its colocalization with TOMM20, a mitochondria marker protein, after 3 h of treatment with CCCP. This translocation declined after 6 h of treatment (Figures 3B and 3C), indicating that PA2G4/EBP1 transiently accumulated in the damaged mitochondria.

Next, to determine the physiological role of PA2G4/EBP1 mitochondria translocation, we treated primary hippocampal neurons from *Nes-Cre; pa2g4*(F/F), which is generated neuron-specific *pa2g4*-conditional knockout mice [18] or *Pa2g4*(+/+) and *pa2g4*(−/−) mouse embryonic fibroblasts (MEFs) with CCCP. We found approximately 50% less mitophagy induction, determined by the number of autolysosomes, in both primary neurons and MEFs, indicating that *pa2g4* deficiency impaired mitophagy induction (Figure 3D and Figure S2B, S2C). To further investigate the involvement of PA2G4/EBP1 in mitophagy induction, we subjected *pa2g4*-CKO and control mice to MCAO and performed a protein ligation assay (PLA). There was a marked increase in PLA signals for TOMM20 and LC3, which reflected the co-occurrence of these proteins and demonstrated mitophagy induction in hippocampal CA1 of control mice. However, we found much less PLA signal in the hippocampus of *pa2g4*-CKO mice, indicating that mitophagy induction was impaired (Figure 3E). In addition,
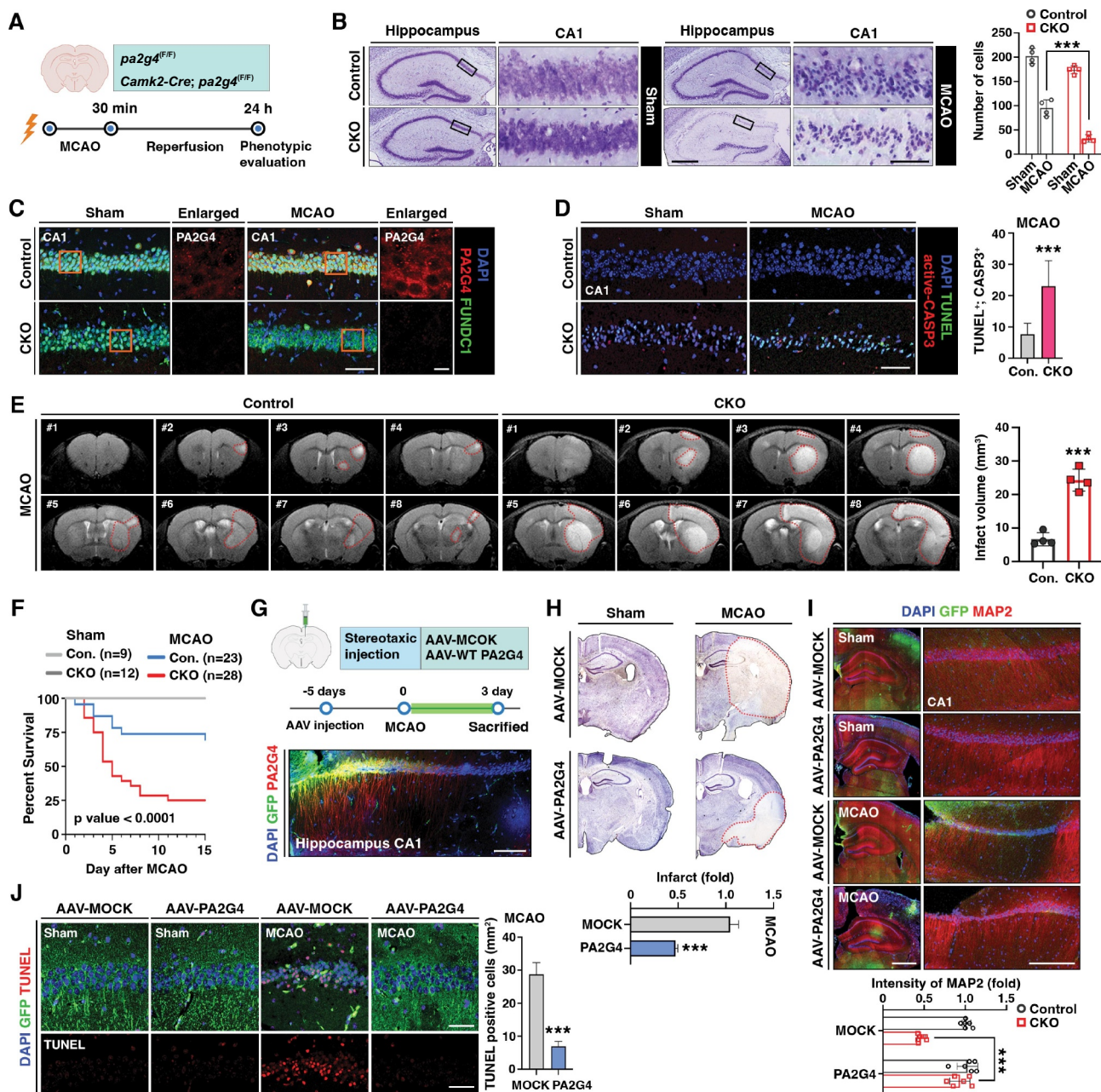
Figure 2. Pa2g4 deficiency exacerbates IR brain injury. (A,B) Diagram of the experimental procedures for inducing ischemic stroke in mice. *pa2g4-CKO* mice and wild-type mice (control) were subjected to 30 min ischemia followed by 24 h of MCAO or sham operation (sham). Brain tissues were subjected to Nissl staining. The number of cells in the CA1 region was quantified and is shown as a bar graph (right side). Scale bars: 200 μm in hippocampus and 50 μm in CA1. (C) Representative images illustrating the histological validation of neuronal cell loss using immunohistochemistry to detect PA2G4 (red) and RBFOX3 (green, marker for neuron) after 24 h reperfusion. White boxes are magnifications. Scale bars: 50 μm for CA1 pictures and 10 μm for the magnified pictures. (D) Representative confocal images (left) and quantification (right) of neuronal death in the CA1 region based on TUNEL (green) and anti-active CASP3 (red) staining after MCAO. The number of TUNEL-positive cells and neuronal cell death data are shown. Scale bars: 50 μm. (E) Infarct volume in *pa2g4-CKO* and control mice was observed using T2-weighted MRI. The infarct volume was quantified and displayed as a bar graph (right). (F) Graph showing the survival percentage of *pa2g4-CKO* or control mice after MCAO and sham operation. The mortality was 95.3% at 1 day and significantly decreased at 5 days (48.7%) after MCAO in *pa2g4-CKO* mice. The following number of mice was sham-operated: n = 9 control and n = 12 *pa2g4-CKO* mice or subjected to MCAO: n = 23 control and n = 28 *pa2g4-CKO* mice. (G) Using a 10-μL Hamilton syringe, AAV2-MOCK or AAV2-PA2G4 were injected into the left CA1 of mice 5 days before MCAO. Viral expression was verified using a fluorescence microscope. Scale bar: 500 μm. (H) Nissl staining of AAV-injected mouse brains after MCAO. The size of the infarct area was measured using ImageJ and is displayed on the bottom. Scale bar: 1 mm. (I) Representative images of GFP and MAP2 (red) staining in ischemic-damaged brains injected with AAV-MOCK or AAV-PA2G4 used to assess neuronal cell death. The intensity of the MAP2 staining was quantified (right panel, n = 6 per group). Scale bar: 500 μm. (J) Representative confocal images (left) and quantification (right) of neuronal death in the CA1 region based on TUNEL (red) and GFP signals in AAV-injected mouse brains after MCAO. TUNEL⁺ indicates the total number of neuronal cell death. Scale bar: 50 μm. All data are presented as means ± SEMs; *p < 0.05, **p < 0.005, ***p < 0.001. Student's two-tailed unpaired t-test (D, E, H, J) and two-way ANOVA with Tukey's post hoc test (B, F, I) were performed.
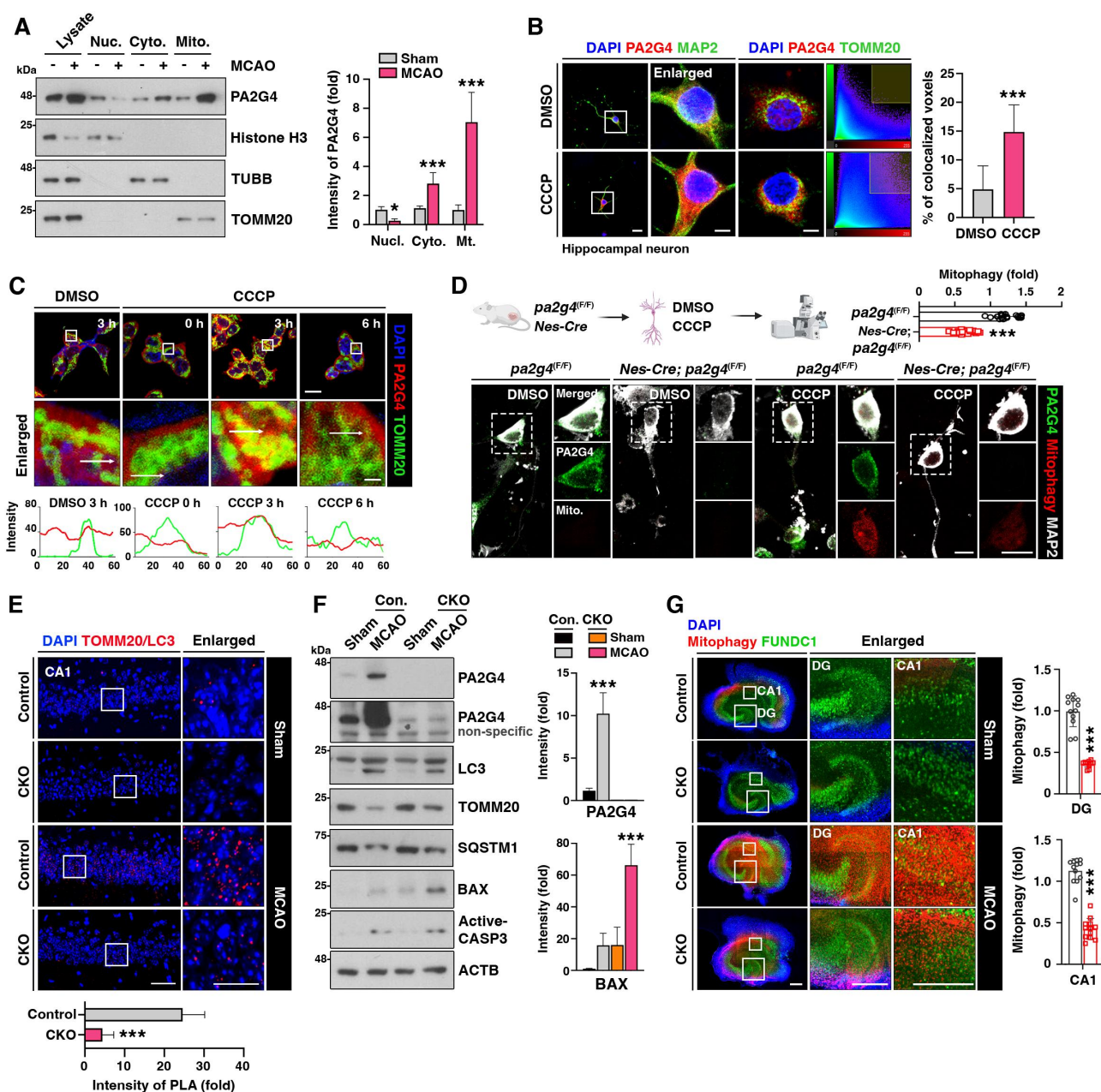
Figure 3. PA2G4 is required in IR-induced mitophagy. (A) Ischemia-damaged hippocampi were separated into nuclear, cytosolic, and mitochondrial fractions. The location of PA2G4 was analyzed using immunoblotting with anti-PA2G4, histone H3 (nucleus), TUBB (cytosol), or TOMM20 (mitochondria) antibodies. A quantitative analysis was performed (right). (B) Primary hippocampal neurons at DIV 7 were treated with CCCP (mitophagy inducer) for 3h and stained using anti-PA2G4 (red), MAP2 (green, left), or TOMM20 (green, right) antibodies. The colocalization between PA2G4 and TOMM20 was analyzed and displayed as a heatmap and bar graph (right). Scale bar: 20 µm. (C) SH-SY5Y cells were treated with CCCP and fixed with 4% PFA after 0, 3, and 6 h. The cells were stained with anti-PA2G4 (red) and TOMM20 (green) antibodies. White boxes are magnifications. The fluorescence intensity of immunolabeled PA2G4/EBP1 and TOMM20 indicated by white arrows is shown as a graph (right). Scale bar: 20 or 5 µm. (D) Primary hippocampal neurons from *Nes-Cre; pa2g4* (F/F) and *pa2g4*(F/F) were treated with CCCP. The neurons were stained with mitophagy dye (red), anti-PA2G4 (green) and MAP2 antibodies. The quantification of mitophagy is shown (top). White boxes are magnifications. Scale bar: 10 µm. (E) In situ Proximity Ligation Assay (PLA) was conducted using anti-TOMM20 and LC3 antibodies. Confocal images of TOMM20–LC3 PLA staining (red) after induced ischemic damage in CA1 are shown. Nuclei were stained using DAPI (blue). The quantification of PLA puncta is shown as a bar graph (bottom). White boxes are magnifications. Scale bar: 50 µm. (F) Mitophagy and apoptosis were analyzed by immunoblotting in the mouse brain after occlusion for 30 min and reperfusion for 24 h using the indicated antibodies. The intensity of PA2G4 and BAX signals was quantified (right panel). (G) Diagram illustrating the experimental time course (left top panel). Hippocampal slice cultures from ischemic-damaged mouse brains were stained using a mitophagy detection kit at DIV 1. Slices were fixed at DIV 3 and stained using an anti-RBFOX3 antibody (green). Mitophagy staining intensity was quantified (left bottom, n = 12 fields per condition). White boxes are magnifications of the DG and CA1 region. Scale bar: 500 µm. All data are presented as means ± SEMs; *p < 0.05, **p < 0.005, ***p < 0.001. Student's two-tailed unpaired t-test (B, D, E, G), one-way ANOVA followed by Bonferroni's post hoc test (F), and two-way ANOVA with Tukey's post hoc test (A) were performed.

immunoblotting confirmed that, compared with that in control mice, MCAO-treated *pa2g4*-CKO brains exhibited reduced mitophagy induction with decreased levels of LC3 and relatively lower TOMM20 signal, whereas there was more cell death with high levels of BAX and active CASP3 (Figure 3F). These data imply that transient mitochondria accumulation of PA2G4/EBP1 upon IR injury is involved in mitophagy induction for neuroprotection.

To clarify whether PA2G4/EBP1 participated in IR-induced mitophagy, we conducted ex vivo cultures of hippocampal slice from ischemic-damaged brains. Indeed, in the absence of PA2G4/EBP1, mitophagy induction was reduced in the hippocampus, including in the dentate gyrus (DG) and CA1, compared with that in the hippocampus of control mice. In contrast, sham treatment did not elicit mitophagy in the hippocampus of either control or *pa2g4*-CKO mice. Therefore, our data suggest that the neuroprotective effect of PA2G4/EBP1 during IR injury results from mitophagy induction (Figure 3G and Figure S2C).

PA2G4/EBP1 is a substrate of PRKN in mitophagy induction.

How does PA2G4/EBP1 function to induce mitophagy after IR injury? PA2G4/EBP1 has been implicated in the ubiquitin–proteasome system by either being a substrate of E3 ligases [31,32] or connecting E3 ligases to their substrates [33,34]. After mitochondria depolarization, PRKN is a key E3 ligase that, in coordination with PTEN-induced kinase 1 (PINK1), triggers mitophagy to eliminate damaged mitochondria. Specifically, PRKN leads to the ubiquitination of substrates on the OMM and utilizes ubiquitin chains as molecular signals to recruit the mitophagy machinery [35]. As a recent proteomic analysis demonstrated that PA2G4/EBP1 is a putative interacting partner of PRKN [36,37], we speculated that PA2G4/EBP1 is involved in PRKN-dependent mitophagy induction. We found a marked ubiquitination of the mitochondrial fraction in the brain of control mice after MCAO, whereas this ubiquitination was dramatically diminished in the *pa2g4*-CKO mouse hippocampus (Figure 4A). Additionally, PA2G4/EBP1 itself was ubiquitinated upon IR injury. PA2G4/EBP1 ubiquitination was particularly intense 24 h after MCAO when PA2G4/EBP1 protein levels and neuroprotective ability peaked. At this time point, mitophagy induction, assessed by increased LC3 signal and decreased SQSTM1 and TOMM20 levels, was also maximal (Figure 4B), implying that the protective effects of PA2G4/EBP1 are related to PRKN-dependent mitochondria degradation.

Accordingly, PA2G4/EBP1 directly bound to PRKN upon mitochondria damage induced by CCCP treatment in neuronal SH-SY5Y cells. In contrast, no interaction between PRKN and PA2G4/EBP1 was observed in the control, vehicle-treated cells (Figure 4C). Ubiquitination assays after cotransfection of glutathione S-transferase (GST)-PA2G4/EBP1 with GFP-PRKN in HEK293 cells showed that PA2G4/EBP1 was ubiquitinated upon mitophagy induction by CCCP treatment, and this ubiquitination was increased by PRKN overexpression, although the levels of ubiquitinated PA2G4/EBP1 were not altered (Figure 4D). Additionally, we confirmed that PRKN-dependent ubiquitination of PA2G4/EBP1 did not elicit proteasomal degradation (Figure 4E). Upon mitophagy induction by CCCP treatment in hippocampal neuronal HT-22 cells, PA2G4/EBP1 accumulated with PRKN in the mitochondria, revealing evident ubiquitination as well as mitophagy induction, determined by increased LC3 and reduced TOMM20 levels (Figures 4F and 4G). Despite the overexpression of GFP-PRKN, *pa2g4*$^{(-/-)}$ MEF cells did not exhibit

mitophagy. However, mitophagy was clearly induced in *Pa2g4*$^{(+/+)}$ MEF cells expressing GFP-PRKN (Figure 4H). Thus, our data suggest that PA2G4/EBP1 is a substrate of PRKN E3 ligase and contributes to PRKN-mediated mitophagy induction.

PRKN-mediated ubiquitination of the lysine (K) 376 in PA2G4/EBP1 contributes to the recruitment of the mitophagy adaptor protein SQSTM1

We identified K373 and K376 as putative ubiquitination sites using the Phosphosite Plus database (Figure S3A) [38]. Subsequently, we generated a PA2G4/EBP1 mutant by substituting K373 or K376 with alanine (A). After mitochondria depolarization induced by 3 h CCCP treatment, PA2G4/EBP1 wild-type (WT) and K373A mutant, but not PA2G4/EBP1^{K376A}, were notably ubiquitinated compared with PA2G4/EBP1 in the control, vehicle-treated group. These observations implied that PA2G4/EBP1 was translocated to the mitochondria and ubiquitinated at K376 in the damaged mitochondria (Figure 5A). In vitro ubiquitination assays performed using purified E1 and E2 ubiquitin ligases, PRKN, and purified WT PA2G4/EBP1 or K376A mutant confirmed that K376 was a residue targeted by PRKN for ubiquitination (Figure 5B). In addition, PA2G4/EBP1 sequence analysis showed that K376 is conserved throughout evolution in many species (Figure S3B). Three-dimensional modeling using the AlphaFold program (https://alphafold.ebi.ac.uk) [39,40] revealed that K376 is located at the exposed helical domain of the protein and supported the notion that K376 could be a potent target site of PRKN E3 ligase (Figure S3C). In contrast to WT PA2G4/EBP1, PA2G4/EBP1^{K376A} mutant, which was not ubiquitinated by PRKN, did not contribute to mitophagy induction and was not localized at the mitochondria (Figure 5C and Figure S3D), implying that PA2G4/EBP1 K376 ubiquitination by PRKN is crucial for mitophagy induction.

PRKN predominantly forms K48- and K63-linked chains during mitophagy [41] to eliminate mitochondrial substrates from the OMM [42] or recruit autophagy receptors, such as SQSTM1, for autophagosome formation, respectively [43-47]. Therefore, we examined the type of ubiquitin chains conjugated on PA2G4/EBP1. In vitro ubiquitination assays demonstrated the presence of K63-linked ubiquitination on PA2G4/EBP1, whereas there was no K48-linked ubiquitination, reflecting the lack of change in PA2G4/EBP1 protein levels upon CCCP-induced mitophagy (Figure 5D, 4th lane). Moreover, siRNA-mediated silencing of PRKN expression abolished the K63-linked ubiquitination of PA2G4/EBP1 in HT-22 cells, confirming that PRKN induced K63 ubiquitination of PA2G4/EBP1 (Figure 5C, 6th lane). Having established that K63 chain ubiquitination of the K376 residue of PA2G4/EBP1 mediated mitophagy induction, we considered whether PRKN ubiquitinated PA2G4/EBP1 to recruit autophagy receptor proteins. Silencing of several mitophagosome receptor proteins, such as SQSTM1, OPTN, and CALCOCO2/NDP52, using siRNAs while simultaneously expressing or not Flag-PA2G4/EBP1 revealed that overexpression of PA2G4/EBP1 could induce mitophagy in the absence of
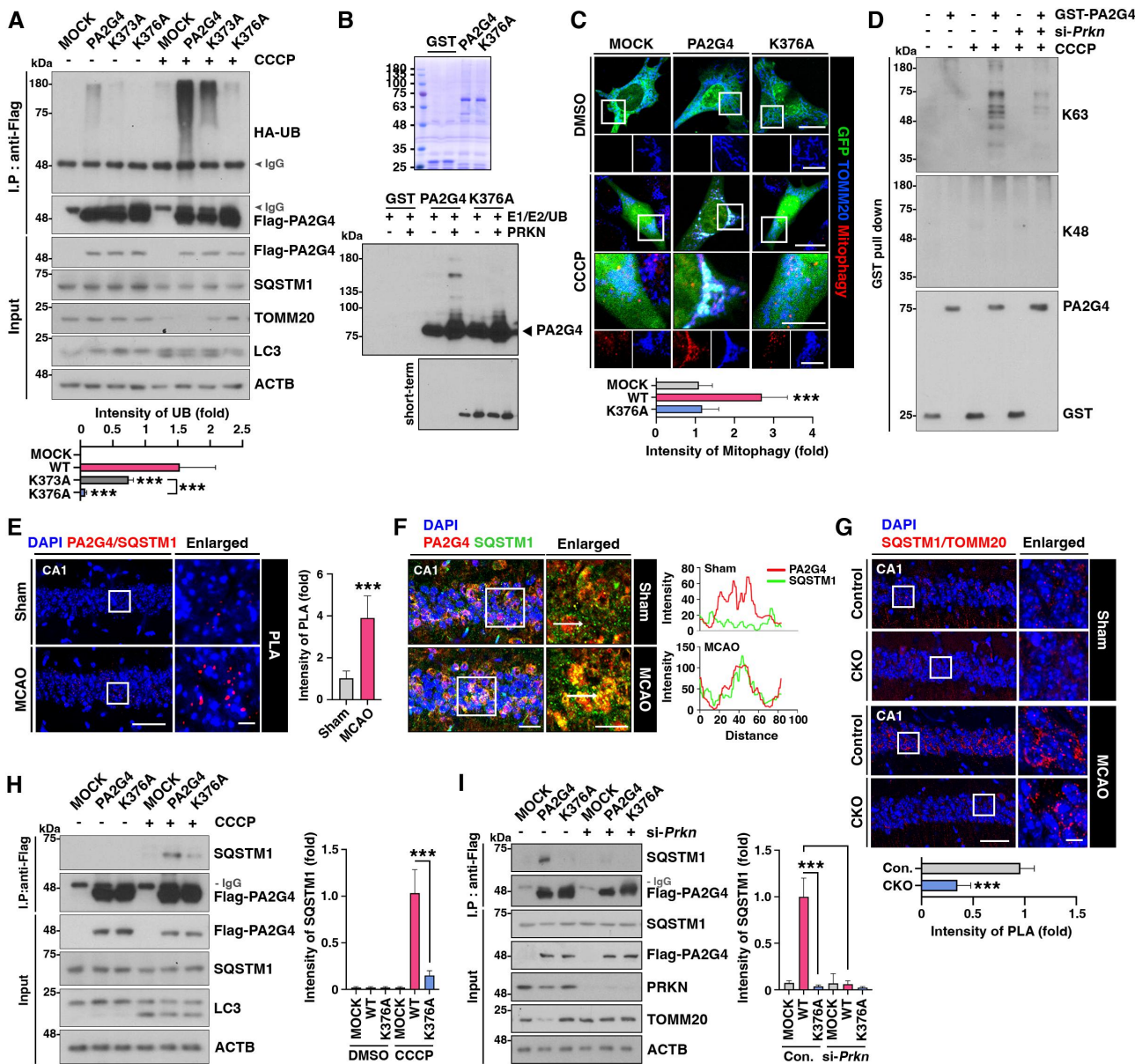
Figure 4. PA2G4 is a substrate of PRKN in mitophagy induction. (A) *pa2g4-CKO* and control mice were subjected to 30 min ischemia followed by 24 h of reperfusion or to a sham operation. Mitochondria were isolated from the hippocampus using a mitochondria fractionation kit (Abcam, #ab110168). Mitochondria ubiquitination was measured by immunoblotting using an anti-ubiquitin (UB) antibody. (B) Brain lysates from sham-operated mice or mice subjected to 30 min ischemia followed by 24, 48, and 72 h of reperfusion were used for immunoprecipitation with an anti-PA2G4 antibody. The ubiquitination of PA2G4 was measured by immunoblotting using an anti-UB antibody. (C) SH-SY5Ycells transfected with GFP-PRKN and/or GST-PA2G4 were treated with CCCP for 3 h. Afterward, a GST pull-down assay was conducted. The binding affinity between GST-PA2G4 and GFP-PRKN with or without CCCP was measured by western blotting. (D) GST pull-down assays were performed on lysates of cells transfected with GST-PA2G4 and/or GFP-together with HA-UB. Ubiquitination of PA2G4 was measured by immunoblotting using an anti-HA antibody. (E) HT-22 cells were transfected with gradient GFP-PRKN. The protein stability of PA2G4 was measured by IB (left) and quantified (right). (F) HT-22 cells were treated with DMSO or CCCP for 3 h and stained with anti-PA2G4 (green), UB (red), and PRKN (blue) antibodies. White boxes are magnifications. The fluorescence intensity of PA2G4, PRKN, and UB signals indicated by orange arrows was quantified (right). Scale bar: 20 μm. (G) HT-22 cells were treated with DMSO or CCCP for 3 h and stained with anti-PA2G4 (green), LC3 (red), and TOMM20 (blue) antibodies. The white boxes are magnifications. The fluorescence intensity of PA2G4, LC3, and TOMM20 signals indicated by orange arrows was quantified (bottom). Scale bar: 20 μm. (H) MEFs from *Pa2g4*[(+/+)] and *pa2g4*[(−/−)] mice were transfected with GFP-MOCK or GFP-PRKN and treated with CCCP for 3 h. Mitophagy was measured using a mitophagy detection kit (red). White boxes are magnifications. The intensity of the mitophagy signal was quantified and is shown as a bar graph (bottom). Scale bar: 10 μm. All data are presented as means ± SEMs; *p < 0.05, **p < 0.005, ***p < 0.001. A two-way ANOVA followed by Tukey's post hoc test (G) was performed.

Figure 5. PRKN-mediated ubiquitination of the K376 residue on PA2G4 contributes to the recruitment of the mitophagy adaptor protein SQSTM1. (A) Flag-MOCK and Flag-WT PA2G4, K373A, and K376A were transfected into HT-22 cells and incubated with CCCP and MG132. Immunoprecipitation of the cell lysates was performed using an anti-Flag antibody to detect ubiquitination of PA2G4 wild-type and mutants. (B) Purified GST-WT PA2G4 and K376A were incubated with E1, E2-UbcH5a, active-PRKN, and UB at 37°C for 1 h. Purified GST, WT PA2G4, and PA2G4^K376A were visualized using Coomassie staining and SDS-PAGE (top). PA2G4 ubiquitination was analyzed by immunoblotting using an anti-PA2G4 antibody (bottom). (C) Transfected HT-22 cells were treated with CCCP and stained with an anti-TOMM20 antibody (green) and mitophagy detection kit (red). White boxes are magnifications. The mitophagy signal intensity was quantified. Scale bar: 20 μm. (D) HT-22 cells were transfected with GST-PA2G4 with or without siRNA targeting *Prkn* (si-*Prkn*) and incubated with CCCP and MG132. After cell lysis, ubiquitination of PA2G4 was analyzed using immunoblotting with anti-K63 and K48 antibodies. (E) PLA was conducted using anti-PA2G4 and SQSTM1 antibodies. Confocal images of PA2G4–SQSTM1 PLA staining (red) after induced ischemic damage in CA1 are shown. Nuclei were stained with DAPI (blue). The quantification of PLA puncta is shown as a bar graph. White boxes are magnifications. Scale bar: 200 μm or 50 μm for the magnifications. (F) Representative immunohistochemistry pictures of ischemic-damaged hippocampus CA1 regions from *pa2g4-CKO* and control mice. Sections were stained with anti-PA2G4 (red) and SQSTM1 (green) antibodies. The fluorescence intensity of PA2G4 and SQSTM1 signals indicated by the white arrows is shown (top). The white boxes are magnifications. Scale bar: 20 or 5 μm. (G) PLA staining of SQSTM1 and TOMM20 in ischemic-damaged brain tissues. Nuclei were stained using DAPI (blue). The quantification of PLA puncta is shown as a bar graph. White boxes are magnifications. Scale bar: 200 μm for CA1 and 50 μm for the magnifications. (H) Flag-WT PA2G4 or K376A were transfected into HT-22 cells, and cells were incubated with CCCP. Binding affinity between PA2G4 and SQSTM1 was measured using western blotting. (I) Flag-WT PA2G4 or K376A and/or si-*Prkn* were transfected into cells and incubated with CCCP and MG132. Cell lysates were subjected to immunoprecipitation, and the interaction affinity between PA2G4 and SQSTM1 was analyzed using immunoblotting. All data are presented as means ± SEMs; *p < 0.05, **p < 0.005, ***p < 0.001. Student's two-tailed unpaired t-test (E, G) and one-way ANOVA with Bonferroni's post hoc test (D) were performed.

OPTN or NDP52. However, when SQSTM1 was depleted, overexpression of PA2G4/EBP1 merely contributed to mitophagy induction (Figure S3E and S3F). Consistent with this observation, PLA demonstrated that the association of PA2G4/EBP1 and SQSTM1 was largely enhanced in the

CA1 region of the brain of MCAO-treated mice (Figure 5E). MCAO resulted in significant mitochondrial accumulation of SQSTM1 in the CA1 of the hippocampus, and over 80% of PA2G4/EBP1-expressing cells colocalized with SQSTM1, suggesting that PA2G4/EBP1 contributed to the recruitment of

SQSTM1 to the damaged mitochondria (Figure 5F). Additionally, in *pa2g4*-CKO mice subjected to MCAO, the binding affinity between SQSTM1 and TOMM20 was decreased compared with that in MCAO-treated control mice (Figure 5G). Furthermore, in SH-SY5Y cells, WT PA2G4/EBP1 but not PA2G4/EBP1^{K376A} mutant, physically interacted with SQSTM1 upon CCCP treatment. Neither WT PA2G4/EBP1 nor PA2G4/EBP1^{K376A} mutant interacted with SQSTM1 in the absence of CCCP (Figure 5H). However, when the expression of PRKN was silenced using siRNAs, WT PA2G4/EBP1 and PA2G4/EBP1^{K376A} failed to interact with SQSTM1 (Figure 5I), regardless of treatment with CCCP. Altogether, these data suggest that under ischemic injury, PA2G4/EBP1 ubiquitinated at K376 by PRKN serves as a linker for recruiting the adaptor protein SQSTM1 in the CA1 region of the hippocampus and contributes to mitophagy induction.

PA2G4/EBP1^{K376} ubiquitination is essential for mitophagy induction and neural protection upon IR injury.

To determine the in vivo effects of PA2G4/EBP1 ubiquitination upon IR injury, we injected AAV2-GFP-PA2G4/EBP1^{K376A} or WT PA2G4/EBP1 into the prospective IR injury site in the mouse brain 5 days before the MCAO operation (Figure 6A and Figure S4A). The brain infarct volume of IR injury shown by MRI was markedly decreased by the overexpression of WT PA2G4/EBP1, but not by that of PA2G4/EBP1^{K376A} mutant, compared with the infarct volume in the control MOCK (Figure 6B). TUNEL analyses showed that neuronal death was highly increased in hippocampi expressing AAV2-GFP-PA2G4/EBP1^{K376A} (~60%) compared with that in hippocampi injected with AAV2-GFP-WT PA2G4/EBP1 (~10%) (Figure 6C and Figure S4B), indicating that the K376A mutation prevented the neuroprotective effects of PA2G4/EBP1 against MCAO in vivo. The immunoreactivity intensity for TOMM20 and SQSTM1 decreased, whereas that of LC3 was increased in mouse brains expressing WT PA2G4/EBP1 after MCAO. In contrast, the immunoreactivity intensities for these markers of mitophagy induction were reversed in the brain of mice expressing PA2G4/EBP1^{K376A} (Figures 6D and 6E). Moreover, in situ PLA signals visualizing the association of SQSTM1 and PA2G4/EBP1 were elevated after MCAO in mouse brains injected with WT PA2G4/EBP1. In contrast, these PLA-positive signals were unchanged after MCAO in mouse brains expressing PA2G4/EBP1 K376A (Figure 6F), indicating that K376 ubiquitination of PA2G4/EBP1 is required for SQSTM1 recruitment and mitophagy induction. Importantly, the brains expressing WT PA2G4/EBP1 after MCAO displayed evident ubiquitination of mitochondria and ubiquitinated PA2G4/EBP1 associated with SQSTM1. In contrast, the brains expressing PA2G4/EBP1^{K376A} following MCAO contained lower ubiquitination levels of mitochondria, and SQSTM1 binding or PA2G4/EBP1 ubiquitination was not detected (Figures 6G and 6H). Hence, PA2G4/EBP1^{K376A} ubiquitination could be the requisite step in mitophagy induction in the early period of MCAO.

The rotarod and open-field tests showed that AAV2-GFP-PA2G4/EBP1 K376A expression did not rescue the mouse locomotor defects, whereas the impaired ambulatory abilities were greatly recovered in AAV2-GFP-WT PA2G4/EBP1-expressing mice compared with those of AAV2-GFP-MOCK-expressing mice (Figures 6I and 6J). In the novel object recognition test, AAV2-GFP-WT PA2G4/EBP1-expressing mice spent more time exploring the novel object (N) than the older one (O1), whereas GFP- PA2G4/EBP1^{K376A} - expressing mice showed no significant difference in the time spent exploring either N or O1, and the exploration times for both objects were similar to that of control, AAV2-GFP-MOCK-expressing mice (Figure 6K). Therefore, the recognition memory that was impaired by MCAO was improved by the expression of WT PA2G4/EBP1 but not by that of PA2G4/EBP1^{K376A}. In the Y-maze test, PA2G4/EBP1^{K376A}-expressing mice subjected to MCAO showed a reduced spontaneous alteration rate (34% reduction) that was similar to that of control mice with MCAO. In contrast, WT PA2G4/EBP1 expression restored this dysfunctional working memory (Figure 6L). Collectively, these data showed that overexpression of PA2G4/EBP1 before IR injury may ameliorate the functional impairments occurring after MCAO, whereas the disruption of PRKN-mediated ubiquitination of PA2G4/EBP1 prevented this beneficial effect of PA2G4/EBP1.

Discussion

Although mitophagy has neuroprotective effects in cerebral ischemia, how it is activated to alleviate neuronal death in the ischemic brain remains unknown. Here, we showed that IR injury induces a transient increase in PA2G4/EBP1 expression and PA2G4/EBP1^{K376A} ubiquitination by PRKN, but depletion of PA2G4 or inhibition of PA2G4/EBP1^{K376A} ubiquitination led to the selective vulnerability of CA1 neurons toward IR injury. The increase in PA2G4/EBP1 levels and K376 ubiquitination preceded or coincided with an increase in the expression of the autophagy marker LC3-II and a decrease in the levels of TOMM20 and the cargo adaptor SQSTM1, which contributed to mitophagy induction. Moreover, we demonstrated that PRKN-mediated PA2G4/EBP1^{K376A} ubiquitination involved K63-linked chains and appeared to regulate mitophagy induction by recruiting SQSTM1 and, subsequently, preventing neuron death at the ischemic injury site (Figure 6M).

Recently, increasing efforts have focused on developing therapeutic strategies for cerebral ischemia to modulate the mitophagy process. Although PA2G4/EBP1 has been implicated as antiapoptotic protein in neurons or certain types of cancers, such as glioblastoma [16,32], its role in cerebral ischemic injury or in the process of mitophagy has not been studied. Our study demonstrates that upregulation of PA2G4/EBP1 in the early period of ischemic damage prevented neuronal death, decreased brain infarct volume, and alleviated motor and cognitive impairments (Figures 6K and 6L). Notably, PA2G4/EBP1 effectively induced mitophagy in the ischemic brain, whereas brain-specific deletion of PA2G4/EBP1 in mice prevented mitophagy induction after MCAO and in CCCP-treated cells (Figures 3C and 3G). Thus, it is conceivable that PA2G4/EBP1 is translocated to the mitochondria upon mitochondrial damage and contributes to
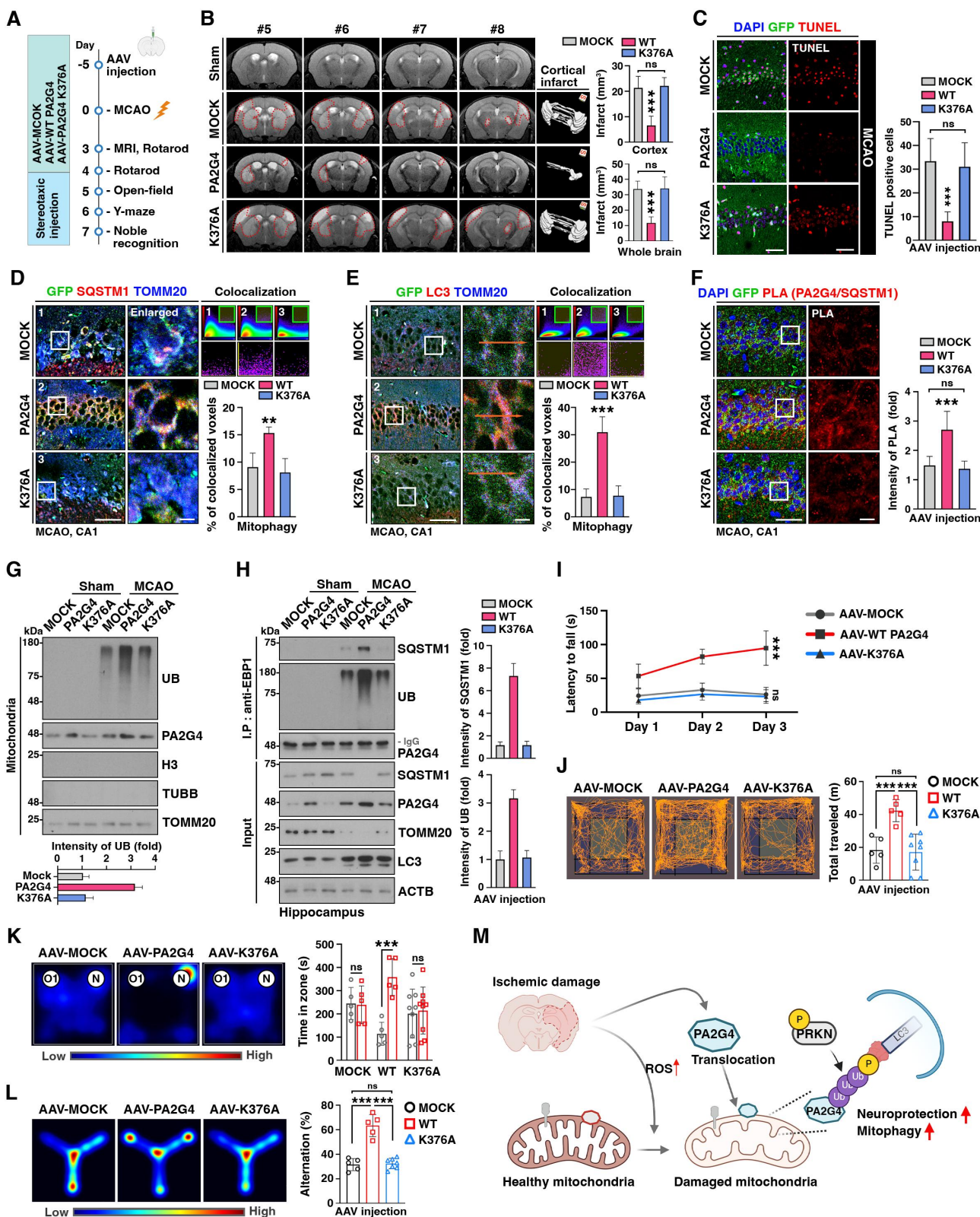
Figure 6. PA2G4^K376 ubiquitination is essential for mitophagy induction and neural protection upon IR injury. (A) Diagram of the experimental procedures used for inducing an ischemic stroke in mice. (B) AAV-MOCK or AAV-WT PA2G4 or K376A were injected into the CA1 region of the hippocampus. The infarct volume was measured after 45 min MCAO using T2-weighted MRI. The red line indicates the boundary of the infarct regions (left). The infarct volume was quantified (right). (C) Representative confocal images (left) and quantification (right) of neuronal death in the CA1 region based on TUNEL (red) staining of AAV-injected mouse brains after MCAO. TUNEL^+ indicates the total number of dead cells and neuronal cell death data are presented. Scale bar: 200 μm. (D, E) Representative immunohistochemistry of ischemic-damaged hippocampus CA1 from *pa2g4-CKO* and control mice. Sections were stained with antibodies specific from SQSTM1 (D, red) or LC3 (E, red) and TOMM20 (blue). White boxes are magnifications. The colocalization was analyzed and displayed as a heatmap and bar graph. Scale bar: 20 μm. (F) AAV-injected mouse brains after stroke were stained with anti-PA2G4 and SQSTM1 antibodies for PLA (red). Nuclei were stained using DAPI (blue). The quantification of PLA puncta is shown as a bar graph. White boxes are magnifications. Scale bar: 200 μm or 50 μm for magnifications. (G) Ubiquitination of mitochondria isolated from AAV-injected brains after MCAO was measured by western blotting using an anti-UB antibody. (H) Brain lysates of AAV-injected MCAO brains were subjected to

mitophagy activation, thus preventing neuronal death in the early period of damage. However, the expression of PA2G4/EBP1 is no longer preserved during sustained IR injury; therefore, hippocampal neurons cannot survive.

In cerebral IR injury, attention has been focused on the PINK-PRKN pathway, which is a known sensor of mitochondria damage. For instance, hypoxic postconditioning-mediated neuroprotection against cerebral ischemia occurs through mitochondria ubiquitination by activated PINK1-PRKN and mitophagy [48]. Mitochondria translocation of PRKN upon mitochondrial damage mediates mitochondrial priming and is a crucial step for preparing the mitochondria for recognition to promote their autophagic removal [49]. Interestingly, PRKN-mediated polyubiquitination on mitochondria leads to OMM protein degradation through the proteasome, and this PRKN-dependent proteasomal removal of OMM proteins is critical for mitophagy [50,51]. Among mitochondria OMM proteins targeted by PRKN, MFN1, and MFN2 are the most susceptible to PRKN-dependent K48-linked ubiquitination and are rapidly degraded after PRKN activation, thereby preventing fusion of damaged mitochondria with healthy ones [52–54]. Moreover, PRKN promotes the proteasomal degradation of phosphorylated RHOT/Miro, quarantining damaged mitochondria prior to their clearance. Thus, PINK1-PRKN activation seems to drive mitochondrial dynamics toward fission by activating pro-fission signaling and inactivating pro-fusion pathways, contributing to mitochondria quality control. On the other hand, PRKN-mediated ubiquitination contributes to the recruitment of ubiquitin-binding autophagy receptors, such as SQSTM1/p62, which is known to connect the ubiquitin system with the autophagic machinery [46]. Autophagy receptors are not recruited to mitochondria in the absence of mitochondrial damage. Once recruited, they initiate mitophagy by assembling autophagosomal membranes to eliminate damaged mitochondria. K63-linked chains have previously been shown to be conjugated by PRKN. An obvious potential role of K63 ubiquitin chains is their recognition by autophagy receptors, including OPTN (optineurin) and SQSTM1/p62 [55–57]. Specifically, preferential binding of SQSTM1 to K63-linked poly-ubiquitin chains on aggregation-prone proteins has been demonstrated in vivo [58–60]. Consistent with these findings, we identified PA2G4/EBP1 as a novel substrate of PRKN on damaged mitochondria after MCAO (Figure 4). PRKN promoted K63-linked ubiquitination of PA2G4/EBP1 K376 (Figures 5A and 5B). This ubiquitination led to PA2G4/EBP1 accumulation at the damaged mitochondria (Figure 4F) and acted as a linker for the adaptor protein SQSTM1, thereby resulting in efficient mitophagy induction. In vivo delivery of PA2G4/EBP1^{K376A} mutant, which cannot be ubiquitinated, prevented mitophagy induction and did not avert the neuronal death and behavioral defects induced by MCAO, indicating that the absence of PRKN-mediated K63-linked ubiquitination on PA2G4/EBP1 hinders the recruitment of adaptor protein SQSTM1 and, subsequently, impairs mitophagy, providing a molecular mechanism underlying the protective effect of PA2G4/EBP1 on neurons during ischemic damage.

Mitochondria dysfunction is involved in multiple pathophysiological processes after cerebral ischemia. As an endogenous adaptive response, mitophagy is known to affect neuronal fate in the ischemic brain through selective mitochondria turnover [61–63]. Here, we used a clinically relevant model of ischemia and proposed a mechanism whereby an increase in PA2G4/EBP1 ubiquitination at K376 by PRKN upon mitochondrial damage promoted mitophagy and attenuated neuronal death (Figure 6). Induction of ischemia triggered a transient increase in PA2G4/EBP1 expression and its translocation to the mitochondria, where PA2G4/EBP1^{K376A} ubiquitination by PRKN occurred, resulting in the recruitment of the adaptor protein SQSTM1 and thereby the activation of mitophagy in neurons before neuronal death. Thus, mitophagy induction promotes neuroprotection in response to ischemic insult.

In summary, we have identified PA2G4/EBP1 as a molecular target of PRKN-mediated mitophagy connected to cerebral IR injury. PRKN-mediated PA2G4/EBP1 ubiquitination was neuroprotective. We further showed an inverse causal relationship between the impairment of PRKN-dependent PA2G4/EBP1 ubiquitination and mitophagy induction as well as neuronal death. Thus, our study proposes that a targeted control of mitophagy during the appropriate time frame is a therapeutic intervention for cerebral ischemia.

Materials and methods

Animals

The mouse *Pa2g4* gene is located on chromosome 10 (NM_011119). *pa2g4*-knockout mice were generated in collaboration with genOway (Lyon, France). To achieve neuron-specific deletion of *pa2g4*, homozygous mutants of the *pa2g4* allele (*pa2g4*$^{flox/flox}$) were crossed with *Camk2-Cre* or *Nes-Cre* mice. All animal experimentations were reviewed and approved by the Institutional Animal Care and Use Committee (IACUC) of Sungkyunkwan University School of Medicine (SUSM, SKKUIACUC 2022-02-27-1). All experimental procedures were performed in accordance with the regulations of the IACUC guidelines of Sungkyunkwan University.

immunoprecipitation using an anti-PA2G4 antibody. The ubiquitination of PA2G4 was measured by immunoblotting using an anti-UB antibody. (I) Locomotion of AAV-injected mice after MCAO analyzed using the accelerated rotarod test; n = 5 for MOCK and WT PA2G4 and n = 9 for PA2G4^{K376A}. (J) Representative maps showing the total distance traveled by AAV-injected mice after MCAO during 10 min in the open-field test (n = 5 for MOCK and WT PA2G4 and n = 8 for PA2G4^{K376A}). (K) Representative heatmaps illustrating the time spent in different locations during the novel object recognition test performed for 10 min. O1, Object 1 or familiar object; N, novel object; n = 5 for MOCK and WT PA2G4 and n = 9 for PA2G4^{K376A}. (L) Representative heatmaps of the mice performance in the Y-maze test. Visiting of arms in the order 1-2-3 is an example of an alternation (AAR); n = 5 for MOCK and WT PA2G4 and n = 9 for PA2G4^{K376A}. (M) Schematic model of PA2G4-PRKN-mediated mitophagy. All data are presented as means ± SEMs; ns > 0.05, *p < 0.05, **p < 0.005, ***p < 0.001. One-way ANOVA with Bonferroni's post hoc test (B–F, K, M) and two-way ANOVA followed by Tukey's post hoc test (L) were performed.

Antibodies

An anti-PA2G4/EBP1 antibody (ab186846) was acquired from Abcam, and another anti-PA2G4/EBP1 antibody (ABE43) was purchased from Sigma-Aldrich. The anti-RBFOX3/NeuN antibody (ABN78) was acquired from Millipore. Anti-SQSTM1/p62 (sc-28359), UB (sc-8017), ACTB/actin (sc-8432), GST (sc-138), GFP (sc-9996), and PRKN/PARKIN (sc-32282) antibodies were obtained from Santa Cruz Biotechnology. Anti-LC3 (ab48394), TOMM20 (ab56783), TIMM23 (ab230253) and HSPD1/HSP60 (ab46798) antibodies were purchased from Abcam, and anti-MAP2 antibody (13-1500) was acquired from Invitrogen.

Transient MCAO

Mice (6–8 weeks old) were anesthetized deeply with isoflurane. Rectal temperature was maintained at 37°C using a feedback-controlled heating system. A midline ventral neck incision was made to expose the common carotid arteries. These arteries were clamped to induce 30 (Figures 2–5) or 45 min (Figures 1 and 6) of ischemia. The clamps were then released for reperfusion. The mice were sacrified immediately after releasing clamps for 0 h MCAO model. The other mice were allowed to survive for 24, 48, and 72 h. Sham control mice underwent the same operation without clamping. Mice were sacrificed and perfused transcardially with saline, followed by 4% paraformaldehyde (PFA) in phosphate-buffered saline (PBS; Gibco, 10010023). The brains were removed, postfixed overnight in a solution containing 4% PFA and 30% sucrose (Duchefa, S0809) in PBS for 48 h. The brains were frozen in an embedding compound (Sakura Finetek, 4583) on dry ice, and coronal sections (20 μm) were cut on a cryostat (Leica CM 1100).

TUNEL staining

TUNEL staining was performed to evaluate cell apoptosis in the mouse hippocampus after ischemic stroke using an In Situ Cell Death Detection Kit (Roche, 11684795910). Brain sections were treated following the procedure specified by the manufacturer.

Viral delivery

Mice (6–8 weeks old) were anesthetized using 5% isoflurane. Isoflurane concentration was maintained at 2% throughout the duration of the surgical procedure. The top of the head was shaved, cleaned with 70% ethanol, and positioned into the stereotactic frame. A midline scalp incision was made, and a small craniotomy was performed using a drill mounted on the frame. Mice were injected with 1 μL of AAV2-MOCK (virus titer: 8.63×10^{12} GC/mL), AAV2-WT PA2G4/EBP1 (virus titer: 2.41×10^{12} GC/mL), or AAV2-K376A (virus titer: 2.77×10^{12} GC/mL) into the left CA1 region of the hippocampus using a 10-μL Hamilton syringe. The stereotaxic coordinates of the injection were: AP: −1.8 mm; ML: −2.0 mm. DV: −1.9 mm.

Immunoprecipitation and immunoblotting

For GST affinity-isolation assays, cells were rinsed with PBS and lysed in buffer containing 50 mM Tris-Cl (Duchefa, T1501), pH 7.4, 150 mM NaCl (Duchefa, S0520), 1 mM EDTA (Sigma, E8008), 0.5% Triton X-100 (Sigma, 93443), 1.5 mM sodium orthovanadate (Sigma, S6508), 50 mM sodium fluoride (Sigma, 201154), 10 mM sodium pyrophosphate (Sigma, 221368), 10 mM beta-glycerophosphate (Sigma, G9422), 1 mM phenylmethylsulfonyl fluoride (Sigma, 52332), and protease cocktail (Calbiochem, 539131). Cell lysates (0.5 to 1 mg of proteins) were incubated with glutathione-sepharose beads (Invitrogen, 10001D) for 3 h at 4°C. Beads were then washed in lysis buffer, mixed with 2× SDS sample buffer, boiled, and analyzed by immunoblotting. Proteins were denatured, resolved by sodium dodecyl sulfate-polyacrylamide gel electrophoresis (SDS-PAGE), and transferred to nitrocellulose membranes (Pall Life Science, 66485). The membranes were blocked using 5% skim milk and incubated sequentially with primary antibodies and horseradish peroxidase-conjugated secondary antibodies (Invitrogen, 31430/31460). All the original images of western blotting are provided in Supplemental Dataset.

Immunostaining and Nissl staining

For IHC, mice were anesthetized and perfused transcardially with saline, followed by 4% paraformaldehyde (PFA). Brains were post-fixed in 4% PFA and incubated with 30% sucrose. Slices were cut and permeabilized using 0.25% Triton X-100 in PBS for 2 h. Then, they were washed and blocked for 1 h in PBS containing 2% bovine serum albumin. Cells were immunostained using primary antibodies overnight and then incubated for 1 h at room temperature with secondary antibodies (Alexa Fluor 488 for green signal or 546 for red signal). The nuclei were counterstained with DAPI. Stained tissues were mounted using a mounting medium (Vector Laboratories, Burlingame, CA, USA). Z-stacked images were acquired using a Zeiss LSM 710 confocal microscope. All images were analyzed with identical parameters using ZEN and ImageJ software [64-67].

For Nissl staining, paraffin-embedded sections were immersed in xylene and rehydrated through a series of decreasing concentrations of ethanol (50%, 70%, 90%, 95%, and 100% ethanol, 3 min each). Sections were washed in PBS and incubated in 0.25% Cresyl Violet acetate for 10 min (Sigma, C5042; dissolved in distilled water with ten drops of glacial acetic acid per 100 mL of solution). After washing in distilled water and dehydration in a series of increasing concentrations of ethanol (50%, 70%, 90%, 95%, and 100% ethanol, 3 min each) and xylene (twice, 3 min each), the sections were mounted using Permount (Fisher Chemical, SP15-100) and left overnight at room temperature. Images were acquired using a slide scanner and analyzed with an Aperio Imagescope (Leica).

Mitophagy

For the quantification of mitophagy, cells were treated with CCCP (Sigma, C2759) and stained with a Mitophagy detection kit (Dojindo Molecular Technologies, MD01) according

to the manufacturer's protocol. The fluorescence intensities of Mtphagy dye (RFP) and Lyso Dye (GFP) were measured using a confocal microscope (LSM 710, Carl Zeiss, Germany).

In situ Proximity Ligation Assay (PLA)

Brains were fixed with 4% PFA, and cryosections were obtained. Following the manufacturer's protocol, primary antibodies were used overnight and secondary antibodies (anti-rabbit PLUS probe and anti-mouse MINUS probe; Sigma, DUO92101) were incubated with the tissues. According to the Duolink protocol, if two proteins are sufficiently close, a rolling circle amplification is triggered by the subsequent additions. Amplified DNA was detected using a specific oligonucleotide that was labeled with a red fluorescence. The tissues were analyzed using a confocal microscope (LSM 710, Carl Zeiss, Germany).

Reverse transcription-quantitative polymerase chain reaction

To compare mRNA levels, RT-qPCRs were performed. Total RNA was isolated from mice using the Takara mini BEST Universal RNA extraction kit (Takara, 9767). Then, cDNA was prepared from total RNA by RT using oligo-dT primers (Takara, 6110A), and qRT-PCR was performed using SsoFast EvaGreen Super Mix (Bio-Rad, 1725201) according to the manufacturer's instruction. Primers specific for the mouse *Gapdh* (5'-GTGTTCCTACCCCC AATGTGT-3', 3'-ATTGTCATACCAGGAAAT-GAGCTT -5') and *Pa2g4* (5'-ATTGATGGAGAGAAGACGATTATC CAGA-ACC-3', 3'-TTTA-AACTGGGCAACAAATTCAC -5') were used for quantifying the expression of *Pa2g4* in the samples. A total reaction mixture of 20 μL was amplified in a 96-well PCR plate (Bio-Rad, HSP9601).

MRI

MRI was performed on a horizontal bore 9.4T/30-cm Burker BioSpec MR system (Billerica, MA, USA) at the Neuroscience Imaging Research (IBS) laboratory at Sungkyunkwan University. Anesthetized animals (1.5% isoflurane in air) were placed in a heated cradle where the temperature was maintained at 37°C. T2-weighted spin-echo images (TR/TE 4 1 5000/50 ms, slice thickness 0.5 mm, 15 slices) across the entire mouse brain were obtained. Mice were blinded to genotype, and the infarct volume was calculated and measured using Horos (Horosproject.org).

Hippocampal slice culture

Mice that underwent MCAO were euthanized. Brain slices of 200 μm thickness were cut in chilled MEMp (50%, vol/vol, minimum essential medium, 25 mM HEPES, and 2 mM glutamine without antibiotics, adjusted to pH 7.2–7.3 with 1 M NaOH) using a vibratome (Leica VT1200, Leica Biosystems). Slices were transferred onto semi-porous membrane inserts (Millipore) in chilled media. Slices were then fixed using 4% PFA in PBS. Fixed slices were washed and collected from the inserted membrane. Mitophagy was assessed using a mitophagy detection kit (DOJINDO, Japan, MD01).

Behavioral testing

All behavioral tests were performed using age- and gender-matched mice.

- Novel object recognition test: The tests were performed in standard mouse cages and consisted of three phases: habituation, familiarization, and test phases. In the habituation phase, mice were placed in an empty mouse cage to adapt to the environment for 10 min. The next day, in the familiarization phase, mice were placed in the same cage with two identical objects, and the time during which the mouse nose touched the object or was oriented toward the object and came within 2 cm of the object was measured for 10 min. In the test phase, which occurred 24 h after the familiarization phase, one of the two objects was replaced with a new object, and the same measurements were recorded for 10 min. The movement of each mouse was recorded and analyzed using the video tracking software EthoVision XT14 (Noldus, Netherlands).

- Y-maze test: We used a symmetrical Y-maze. Each mouse was placed in one arm with a side wall and allowed to explore the maze for 10 min. The movement of each mouse was recorded and analyzed using the video tracking software EthoVision XT14 (Noldus, Netherlands).

- Open-field test: The open field test was used to assess anxiety and exploratory behaviors. Each mouse was placed near the wall of the open field area (44.5 × 44.5 cm). The area was separated into two zones: the center (28.5 × 28.5 cm) and the periphery. The open field test was performed for 20 min. The movements of the mice were recorded and analyzed automatically using the animal activity meter Opto-Varimex -5 Auto-Track (Columbus, OH, USA).

- Rotarod test: An accelerating rotarod (Ugo Basile, Italy) was used to assess motor coordination and balance. Mice were placed on the cylinder, which slowly accelerated from 4 to 40 rpm over a 5-min test session. The task required the mice to walk to remain on top of the rotating rod.

Statistical analysis

The analysis of all data was performed with two-tailed Student's t-test, one-way ANOVA by Bonferroni's post hoc test or twe-way ANOVA accompanied by Tukey's post hoc analyses (GraphPad Prism 9). All data representative of three independent experiments are presented as the mean ± SEM. *P < 0.05; **P < 0.01; ***P < 0.001; ns, not significant. Fluorescence intensity, puncta number and Pearson's correlation coefficients were calculated using ImageJ software (2.9.0). Colocalization for mitophagy was measured using Imaris software 10.

Disclosure statement

Funding

References

1. Kirino T, Sano K. Fine structural nature of delayed neuronal death following ischemia in the gerbil hippocampus. Acta Neuropathol. 1984;62:209–18.
2. Vosler PS, Gao Y, Brennan CS, et al. Ischemia-induced calpain activation causes eukaryotic (translation) initiation factor 4G1 (eIF4GI) degradation, protein synthesis inhibition, and neuronal death. Proc Natl Acad Sci U S A. 2011;108:18102–7.
3. Tanaka K, Ludwig LM, Krolikowski JG, et al. Isoflurane produces delayed preconditioning against myocardial ischemia and reperfusion injury: role of cyclooxygenase-2. Anesthesiology. 2004;100:525–31.
4. Livingston MJ, Wang J, Zhou J, et al. Clearance of damaged mitochondria via mitophagy is important to the protective effect of ischemic preconditioning in kidneys. Autophagy 2019;15:2142–62.
5. Yuan Y, Zheng Y, Zhang X, et al. BNIP3L/NIX-mediated mitophagy protects against ischemic brain injury independent of PARK2. Autophagy 2017;13:1754–66.
6. Zhang J. Autophagy and Mitophagy in Cellular Damage Control. Redox Biol 2013;1:19–23.
7. Wu R, Li X, Xu P, et al. TREM2 protects against cerebral ischemia/reperfusion injury. Molecular Brain 2017;10:20.
8. Chen C, Gao JL, Liu MY, et al. Mitochondrial fission inhibitors suppress endothelin-1-induced artery constriction. Cell Physiol Biochem 2017;42:1802–11.
9. Zhang J. Autophagy and Mitophagy in Cellular Damage Control. Redox Biol 2013;1:19–23.
10. López-Doménech G, Howden JH, Covill-Cooke C, et al. Loss of neuronal Miro1 disrupts mitophagy and induces hyperactivation of the integrated stress response. The EMBO Journal 2021;40: e100715.
11. Galluzzi L, Kepp O, Kroemer G. Mitochondrial regulation of cell death: a phylogenetically conserved control. Microb Cell 2016;3:101–8.
12. Yuan Y, Rangarajan P, Kan EM, et al. Scutellarin regulates the Notch pathway and affects the migration and morphological transformation of activated microglia in experimentally induced cerebral ischemia in rats and in activated BV-2 microglia. J Neuroinflammation. 2015;12:11.
13. Wang J, Zhou H. Mitochondrial quality control mechanisms as molecular targets in cardiac ischemia–reperfusion injury. Acta Pharmaceutica Sinica B 2020;10:1866–79.
14. Wu Y, Liu H, Wang X. Cardioprotection of pharmacological postconditioning on myocardial ischemia/reperfusion injury. Life Sci 2021;264:118628.
15. Nguyen et al., 2016
16. Liu Z, Ahn JY, Liu X, et al. Ebp1 isoforms distinctively regulate cell survival and differentiation. Proc Natl Acad Sci U S A 2006;103:10917–22.
17. Ko HR, Hwang I, Ahn SY, et al. Neuron-specific expression of p48 Ebp1 during murine brain development and its contribution to CNS axon regeneration. BMB Rep 2017;50:126–31.
18. Ko HR, Hwang I, Jin EJ, et al. Roles of ErbB3-binding protein 1 (EBP1) in embryonic development and gene-silencing control. Proc Natl Acad Sci U S A 2019;116:24852–60.
19. Hwang I, Ko HR, Ahn J-Y. The roles of multifunctional protein ErbB3 binding protein 1 (EBP1) isoforms from development to disease. Experimental & Molecular Medicine 2020;52:1039–47.
20. Hwang I, Ahn JY. Dysregulation of Epigenetic Control Contributes to Schizophrenia-Like Behavior in Ebp1(+/-) Mice. Int J Mol Sci 2020; 21.
21. Kim BS, Ko HR, Hwang I, et al. EBP1 regulates Suv39H1 stability via the ubiquitin-proteasome system in neural development. BMB Rep 2021;54:413–8.
22. Hwang I, Kim BS, Ko HR, et al. Cerebellar dysfunction and schizophrenia-like behavior in Ebp1-deficient mice. Mol Psychiatry 2022;27:2030–41.
23. Stamova B, Jickling GC, Ander BP, et al. Gene expression in peripheral immune cells following cardioembolic stroke is sexually dimorphic. PLoS One 2014;9:e102550.
24. Carlsson R, Özen I, Barbariga M, et al. STAT3 precedes HIF1α transcriptional responses to oxygen and oxygen and glucose deprivation in human brain pericytes. PLoS One 2018;13: e0194146.
25. Liu Y, Shoji-Kawata S, Sumpter RM, Jr., et al. Autosis is a Na+,K +-ATPase-regulated form of cell death triggered by autophagy-inducing peptides, starvation, and hypoxia-ischemia. Proc Natl Acad Sci U S A 2013;110:20364–71.
26. Tsien JZ, Huerta PT, Tonegawa S. The essential role of hippocampal CA1 NMDA receptor-dependent synaptic plasticity in spatial memory. Cell 1996;87:1327–38.
27. Dragatsis I, Zeitlin S. CaMKIIalpha-Cre transgene expression and recombination patterns in the mouse brain. Genesis 2000;26:133–5.
28. Shen S, Horowitz ED, Troupes AN, et al. Engraftment of a galactose receptor footprint onto adeno-associated viral capsids improves transduction efficiency. J Biol Chem 2013;288:28814–23.
29. Aschauer DF, Kreuz S, Rumpel S. Analysis of transduction efficiency, tropism and axonal transport of AAV serotypes 1, 2, 5, 6, 8 and 9 in the mouse brain. PLoS One 2013;8:e76310.
30. Liu L, Sakakibara K, Chen Q, et al. Receptor-mediated mitophagy in yeast and mammalian systems. Cell Research 2014;24:787–95.
31. Liu C, van Dyk D, Li Y, et al. A genome-wide synthetic dosage lethality screen reveals multiple pathways that require the functioning of ubiquitin-binding proteins Rad23 and Dsk2. BMC Biology 2009;7:75.
32. Wang Y, Liu X, Zhou L, et al. Identifying the ubiquitination targets of E6AP by orthogonal ubiquitin transfer. Nature Communications 2017;8:2232.
33. Kim CK, Nguyen TL, Joo KM, et al. Negative regulation of p53 by the long isoform of ErbB3 binding protein Ebp1 in brain tumors. Cancer Res 2010;70:9730–41.
34. Ko HR, Kim CK, Lee SB, et al. P42 Ebp1 regulates the proteasomal degradation of the p85 regulatory subunit of PI3K by recruiting a chaperone-E3 ligase complex HSP70/CHIP. Cell Death Dis 2014;5:e1131.
35. Gladkova C, Maslen SL, Skehel JM, et al. Mechanism of parkin activation by PINK1. Nature 2018;559:410–4.
36. Hosp F, Vossfeldt H, Heinig M, et al. Quantitative interaction proteomics of neurodegenerative disease proteins. Cell Rep 2015;11:1134–46.
37. Sun X, Hong Y, Shu Y, et al. The involvement of Parkin-dependent mitophagy in the anti-cancer activity of Ginsenoside. J Ginseng Res 2022;46:266–74.
38. Hornbeck PV, Zhang B, Murray B, et al. PhosphoSitePlus, 2014: mutations, PTMs and recalibrations. Nucleic Acids Res 2015;43: D512–20.
39. Jumper J, Evans R, Pritzel A, et al. Highly accurate protein structure prediction with AlphaFold. Nature 2021;596:583–9.

40. Tunyasuvunakool K, Adler J, Wu Z, et al. Highly accurate protein structure prediction for the human proteome. Nature 2021;596:590–6.

41. Ordureau A, Sarraf SA, Duda DM, et al. Quantitative proteomics reveal a feedforward mechanism for mitochondrial PARKIN translocation and ubiquitin chain synthesis. Mol Cell 2014;56:360–75.

42. Yoshii SR, Kishi C, Ishihara N, et al. Parkin mediates proteasome-dependent protein degradation and rupture of the outer mitochondrial membrane. J Biol Chem 2011;286:19630–40.

43. Richard TJC, Herzog LK, Vornberger J, et al. K63-linked ubiquitylation induces global sequestration of mitochondria. Scientific Reports 2020;10:22334.

44. Ham SJ, Lee D, Yoo H, et al. Decision between mitophagy and apoptosis by Parkin via VDAC1 ubiquitination. Proc Natl Acad Sci U S A 2020;117:4281–91.

45. Sarraf SA, Raman M, Guarani-Pereira V, et al. Landscape of the PARKIN-dependent ubiquitylome in response to mitochondrial depolarization. Nature 2013;496:372–6.

46. Geisler S, Holmström KM, Skujat D, et al. PINK1/Parkin-mediated mitophagy is dependent on VDAC1 and p62/SQSTM1. Nat Cell Biol 2010;12:119–31.

47. Palikaras K, Lionaki E, Tavernarakis N. Mechanisms of mitophagy in cellular homeostasis, physiology and pathology. Nat Cell Biol 2018;20:1013–22.

48. Wen H, Li L, Zhan L, et al. Hypoxic postconditioning promotes mitophagy against transient global cerebral ischemia via PINK1/Parkin-induced mitochondrial ubiquitination in adult rats. Cell death & disease, 2021:630.

49. Ding WX. Role of autophagy in liver physiology and pathophysiology. World J Biol Chem 2010;1:3–12.

50. Chan NC, Salazar AM, Pham AH, et al. Broad activation of the ubiquitin-proteasome system by Parkin is critical for mitophagy. Hum Mol Genet 2011;20:1726–37.

51. Kim SJ, Syed GH, Siddiqui A. Hepatitis C virus induces the mitochondrial translocation of Parkin and subsequent mitophagy. PLoS Pathog 2013;9:e1003285.

52. Gegg ME, Cooper JM, Chau KY, et al. Mitofusin 1 and mitofusin 2 are ubiquitinated in a PINK1/parkin-dependent manner upon induction of mitophagy. Hum Mol Genet 2010;19:4861–70.

53. Glauser L, Sonnay S, Stafa K, et al. Parkin promotes the ubiquitination and degradation of the mitochondrial fusion factor mitofusin 1. J Neurochem 2011;118:636–45.

54. Rakovic A, Grünewald A, Kottwitz J, et al. Mutations in PINK1 and Parkin impair ubiquitination of Mitofusins in human fibroblasts. PLoS One 2011;6:e16746.

55. Narendra D, Kane LA, Hauser DN, et al. p62/SQSTM1 is required for Parkin-induced mitochondrial clustering but not mitophagy; VDAC1 is dispensable for both. Autophagy 2010;6:1090–106.

56. van Wijk SJL, Melquiond ASJ, de Vries SJ, et al. Dynamic control of selectivity in the ubiquitination pathway revealed by an ASP to GLU substitution in an intra-molecular salt-bridge network. PLOS Computational Biology 2012;8:e1002754.

57. Wong YC, Holzbaur EL. Optineurin is an autophagy receptor for damaged mitochondria in parkin-mediated mitophagy that is disrupted by an ALS-linked mutation. Proc Natl Acad Sci U S A 2014;111:E4439–48.

58. Babu JR, Geetha T, Wooten MW. Sequestosome 1/p62 shuttles polyubiquitinated tau for proteasomal degradation. J Neurochem 2005;94:192–203.

59. Long J, Gallagher TR, Cavey JR, et al. Ubiquitin recognition by the ubiquitin-associated domain of p62 involves a novel conformational switch. J Biol Chem 2008;283:5427–40.

60. Seibenhener ML, Babu JR, Geetha T, et al. Sequestosome 1/p62 is a polyubiquitin chain binding protein involved in ubiquitin proteasome degradation. Mol Cell Biol 2004;24:8055–68.

61. Geisler S, Holmström KM, Skujat D, et al. PINK1/Parkin-mediated mitophagy is dependent on VDAC1 and p62/SQSTM1. Nat Cell Biol 2010;12:119–31.

62. Lamark T, Svenning S, Johansen T. Regulation of selective autophagy: the p62/SQSTM1 paradigm. Essays Biochem 2017;61:609–24.

63. Guan Q, Zhou LL, Li YA, et al. diiodo-bodipy-encapsulated nanoscale metal-organic framework for pH-driven selective and mitochondria targeted photodynamic therapy. Inorg Chem 2018;57:10137–45.

64. Shao Z, Dou S, Zhu J, et al. The role of mitophagy in ischemic stroke. Front Neurol 2020;11:608610.

65. Kim CK, Hwang JY, Hong TH, et al. Combination stem cell therapy using dental pulp stem cells and human umbilical vein endothelial cells for critical hindlimb ischemia. BMB Rep 2022;55:336–41

66. Lee S, Lee S, Lee SJ, et al. Inhibition of mitoNEET induces Pink1-Parkin-mediated mitophagy. BMB Rep 2022;55:354–9.

67. Ryu YC, Kim YR, Park J, et al. Wnt/β-catenin signaling activator restores hair regeneration suppressed by diabetes mellitus. BMB Rep 2022;55:559–64.